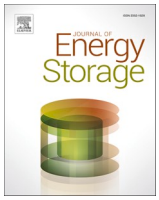
Journal of Energy Storage 183 (2027) 125365



Contents lists available at ScienceDirect

Journal of Energy Storage

journal homepage: www.elsevier.com/locate/est



Research papers

A novel method for mechanical battery abuse testing: Planetary mill calorimetric evaluation of all-solid-state battery materials and their safety

Florian Salk [a,*], Thomas Bayha [a], Sebastian Scharner [b], Philipp Heugel [a], Martin Miller [a], Thomas Berger [a], Franziska Klein [a], Jens Tübke [a,c]

[a] Fraunhofer Institute for Chemical Technology ICT, Joseph-von-Fraunhofer-Straße 7, Pfinztal, 76327, Germany
[b] BMW Group, Battery Cell Technology, Predevelopment - Requirements and Concepts, Lerchenauer Straße 76, Munich, 80788, Germany
[c] Institute of Mechanical Process Engineering and Mechanics (MVM), Karlsruhe Institute of Technology (KIT), Straße am Forum 8, Karlsruhe, 76131, Germany

ARTICLE INFO

Keywords:
All-solid-state batteries
Mechanical abuse
Safety testing
Calorimetry
Sulfide electrolyte
Thermal runaway

ABSTRACT

This work presents a novel quantitative calorimeter-mill methodology for ASSB materials that quantitatively measures energy release by combining ball milling with calorimetry and pressure monitoring during extreme mechanical activation. The method accounts for the mechanical milling contribution using an operational reference. Applied to a shredded cathode consisting of delithiated state of charge 100% (SOC 100) Li_x-$Ni_{0.83}Mn_zCo_{0.17-z}O_2$ ($x < 1$, $z < 0.17$) (NMC), Al current collector, binder and conductive carbon together with systematically chosen amounts of Li_6PS_5Cl representing different catholyte compositions, the method quantifies composition-dependent energy release and gas evolution under extreme mechanical abuse. The method revealed that a shredded, delithiated NMC cathode showed substantial reactivity (2799 ± 159 J/$g_{(NMC)}$) with significant gas evolution, while Li_6PS_5Cl electrolyte addition enhanced the energy release and reduced the required mechanical activation and the gas generation. The calorimeter-mill approach provides a quantitative framework for establishing worst-case energy boundaries and enabling early-stage safety decisions in battery material development.

1. Introduction

Battery safety evaluation is fundamental for the development and commercialization of next-generation energy storage systems [1,2], particularly as the automotive industry advances toward electrification [3–5]. International standards classify battery safety tests mostly into three primary categories [4,6]: electrical-abuse (e.g. overcharge, short circuit), thermal-abuse (e.g. overheating, accelerated rate calorimetry (ARC)), and mechanical-abuse (e.g. penetration, crush, impact), as defined amongst others in UN 38.3 [7], IEC 62133–2 [8], and SAE J2464 [9]. Recent regulatory updates, including China's GB 38031–2025 [10] and India's AIS-156 amendments(1–4) [11], emphasize comprehensive abuse testing with particular focus on thermal propagation [6], reflecting the critical importance of understanding worst-case failure scenarios.

All-solid-state batteries (ASSBs) represent a transformative approach to energy storage [12–14], replacing flammable liquid electrolytes with solid-electrolytes [15]. This fundamental change in cell architecture offers several advantages including enhanced energy density [16], wider operating temperature ranges [17,18], and simplified thermal management [13]. However, the distinct mechanical and chemical properties of solid electrolytes (SE) - ranging from brittle ceramics [19], crystalline and glassy sulfides [20,21] to relatively soft polymers [22] – necessitate adapted safety evaluation methodologies beyond those established for conventional lithium-ion batteries (LIBs) [6].

Current ASSB safety research has predominantly focused on thermal-abuse mechanisms [23,24] and DSC studies [20,25–27], revealing important insights into temperature-induced degradation pathways. Studies mostly beginning in 2017 demonstrated that sulfide electrolytes can undergo exothermic reactions with delithiated cathode materials at elevated temperatures [28–32]. Tsukasaki et al. [28,29] identified exothermic transition-metal-sulfide formation when Li_3PS_4 electrolytes contact charged NMC cathodes above 200 °C, while subsequent investigations quantified decomposition enthalpies and visualized thermal

* Corresponding author.
E-mail addresses: florian.salk@ict.fraunhofer.de (F. Salk), thomas.bayha@ict.fraunhofer.de (T. Bayha), sebastian.scharner@bmw.de (S. Scharner), philipp.heugel@ict.fraunhofer.de (P. Heugel), martin.miller@ict.fraunhofer.de (M. Miller), thomas.berger@ict.fraunhofer.de (T. Berger), franziska.klein@ict.fraunhofer.de (F. Klein), jens.tuebke@ict.fraunhofer.de (J. Tübke).

https://doi.org/10.1016/j.est.2026.125365
Received 2 June 2026; Received in revised form 7 September 2026; Accepted 24 October 2026
Available online 2 November 2026
2352-152X/© 2026 The Authors. Published by Elsevier Ltd. This is an open access article under the CC BY license (http://creativecommons.org/licenses/by/4.0/).
Open access funding enabled and organized by Projekt DEAL.

runaway through operando techniques [33]. Previous studies have demonstrated mechanically induced reactions between charged NMC and sulfide electrolytes [32,34]. These findings established that while solid electrolytes eliminate certain hazards associated with liquid systems, they introduce distinct failure modes requiring specialized characterization.

Despite growing understanding of thermal degradation, mechanical-abuse scenarios remain not fully understood [4,35]. A nail penetration test serves as the primary mechanical-abuse standard [36], providing pass/fail criteria and enabling some calorimetric assessment when performed in an autoclave calorimetry setup [37]. However, nail penetration outcomes depend strongly on multiple parameters - insertion angle, speed, depth of the nail, nail material and diameter making systematic comparison challenging [38]. Moreover, the localized nature of penetration may not access the full reaction potential of the battery materials [38]. A complementary approach that enables thorough mixing could provide upper-bound energy release values, establishing worst-case scenarios for safety design. The calorimeter-mill is therefore not intended to reproduce a specific cell-level mechanical-abuse event, but to provide controlled extreme mechanical activation for quantifying material-level worst-case energy-release boundaries.

Here, we introduce a calorimeter-mill approach that accounts for the operational mechanical contribution when estimating chemical energy release during such activation. The method combines mechanical ball milling with calorimetry to quantitatively assess energy release. Ball milling creates high interfacial contact between reactive components (e.g. sulfide based solid electrolytes & cathode material) while the calorimetric system captures the thermal response, and a pressure sensor monitors the gas evolution of chemical reactions. By quantifying and subtracting an operational mechanical reference, the method estimates the net chemical energy release. This approach enables early-stage screening of material compositions before costly cell fabrication [13], providing experimentally reliable quantitative data for go/no-go decisions in battery development.

Li_6PS_5Cl exhibits particularly promising characteristics as a solid electrolyte [39], including high ionic conductivity (>1 mS/cm) [40], low grain-boundary resistance [22], mechanical processability [41], and potential for cost-effective production [42]. NMC cathodes offer superior energy density compared to alternatives like $LiFePO_4$ (LFP) [13,43] while maintaining lower cost than $LiCoO_2$ (LCO) [15], making them prevalent in current automotive applications [13,44].

Accordingly, this study aims to establish and validate the calorimeter-mill methodology and to determine whether and how the Li_6PS_5Cl content influences energy release and gas evolution under the defined calorimeter-mill conditions in delithiated NMC cathodes, including the current collector, binder, and conductive carbon.

2. Methods & materials

2.1. Materials

The sulfide-based solid electrolyte (Li_6PS_5Cl, ≥99.5% purity, battery grade) was purchased from Sigma-Aldrich and used as received.

The delithiated NMC material ($Li_xNi_{0.83}Mn_zCo_{0.17-z}O_2$ ($x < 1$, $z < 0.17$), SOC 100) was sourced from an industrial automotive partner in the form of coated aluminum foil electrodes which were extracted from fully charged batteries (cut-off voltage 4.2 V), washed thoroughly with dimethyl-carbonate (DMC), and shredded into fine particles while still adhered to the aluminum current collector. This approach, using complete electrodes, includes interactions between all cathode components under mechanical-abuse conditions, thereby providing a more realistic assessment than experiments using isolated electrode components.

2.2. Differential scanning calorimetry

Differential scanning calorimetry (DSC) was performed using a Q2000 calorimeter (TA Instruments, New Castle, USA). Samples were hermetically sealed in high-pressure stainless-steel crucibles (Model F20, Mettler-Toledo, Greifensee, Switzerland) with a nominal volume of 20 µL and a defined closing force of 4 kN. In contrast to the samples used for the calorimeter-mill experiments, to ensure homogeneity despite the small sample masses required for reliable DSC measurements (1.460, 2.038, and 1.391 mg), the electrode material (NMC, conductive carbon, and binder) was mechanically separated from the aluminum current collector, weighed, mixed with Li_6PS_5Cl, and transferred into the crucibles inside an argon-filled glovebox. The sealed crucibles were then heated from room temperature to 550 °C at a constant rate of 5 K/min. Heat flow was recorded continuously.

2.3. Calorimeter-mill

The focus of this work is the establishment, validation, and application of a calorimeter-mill methodology for quantitative mechanical-abuse calorimetry.

2.3.1. Setup

The experimental setup consists of a custom-designed calorimeter-mill system that combines mechanical ball milling capabilities with thermal and pressure monitoring as shown in Fig. 1. The system utilizes a planetary ball mill (Pulverisette 7 Premium Line, FRITSCH GmbH, Idar-Oberstein, Germany) equipped with an “easy GTM” grinding bowl (FRITSCH GmbH, Idar-Oberstein, Germany). The EASY GTM system integrates pressure and temperature sensing into the lid-mounted measuring/transmission unit. The pressure sensor is connected to the grinding-bowl headspace through openings in the lid, whereas the temperature sensor is located within the measuring/transmission unit. The specific sensor technologies are not specified by the manufacturer. The measured data are transmitted wirelessly to the ball mill control unit at a sampling frequency of 0.38 Hz. Due to the sensor position and thermal inertia of the lid assembly, a certain response delay is expected for the temperature measurement.

For the mechanical grinding, ZrO_2 -balls were employed, providing sufficient mechanical energy for material mixing and reaction initiation. To enable accurate calorimetric measurements, a custom insulation chamber of mainly extruded polystyrene foam housed in a polypropylene container was tailored to the GTM grinding bowl.

2.3.2. Calorimetric characterization

To characterize the calorimetric system, a thorough assessment of its thermal properties was performed.

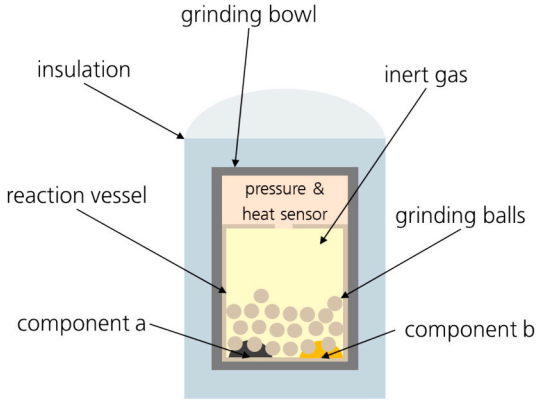


Fig. 1. Schematic of the complete calorimeter including insulation and integrated pressure/temperature sensing.

2.3.2.1. Heat capacity determination. For the following heat-capacity, heat-loss, and energy-accounting analysis, a consistent notation is required. The symbols and parameters used throughout the calorimetric characterization and subsequent equations are summarized in Table 1.

The heat capacity of the milling bowl (Fig. 1) was determined via a dewar-bath experiment conducted in a climate chamber set to 23 °C. To bracket the full operating window (8–38 °C) around the chamber set-point (23 °C), a total mass of 1900 g of deionized water in the dewar was cooled to 8 °C with deionized ice and allowed to equilibrate. The bath was then continuously heated above 38 °C. Continuous magnetic stirring at 400 rotations per minute (rpm) maintained temperature homogeneity. For heating, electric energy was supplied via a flexible polyimide and etched CuNi44 heating foil (WoF 50060 type, J Winkler GmbH, Heidelberg, Germany) directly in the water and quantified using a four-point measurement system to determine voltage, current, and time ($E = U{\cdot}I{\cdot}t$). Temperature evolution was monitored using four Pt-100 sensors (Pt100A 20/050/NB/4 Cu TT17/2 m, Electronic Sensor GmbH, Heilbronn, Germany) positioned on the milling bowl within the water bath. Voltage, current and time were logged, using a Yokogawa GM10 with GX90XA-10-U2NCN module (Yokogawa Europe B.V., Amersfoort, Netherlands). Eight independent measurements were performed: first four times with water alone to establish the dewar-water-system heat capacity, and subsequently four times with the calorimeter bowl (sealed in waterproof plastic foil) immersed in the water bath. Uncertainties of differences were propagated by root-sum-of-squares (RSS) assuming independence (1σ).

The heat capacity calculations of the empty **calorimeter bowl** yielded 8502.4 ± 5.2 J/K for the system without the bowl and 9094.9 ± 4.4 J/K with the bowl included ($n = 4$). The difference of **592.4 ± 6.8 J/K** represents the heat capacity contribution of the bowl.

To account for the **ZrO_2 grinding balls** used during experiments, their heat capacity was calculated based on their material properties (specific heat capacity: 0.55 [45]: J/(g·K) for ZrO_2 with 3.5% MgO, density: 5.7 [45] g/mL). For a total volume of 10.47 mL (± 0.05 mL (estimated deviation due to manufacturing tolerances), this adds **32.8 ± 1.6 J/K**.

The **insulation** requires special consideration. The extruded polystyrene foam insulation has a total heat capacity of 106.6 ± 1.1 J/K ((75.91 ± 0.01 g) • 1.404 [46] J/(g·K)). However, during measurements, the insulation exhibits a temperature gradient from room temperature at the outer surface to the calorimeter temperature at the inner surface. Assuming linear temperature distribution through the insulation cross section, the effective heat capacity contribution is half of the total value, yielding **53.3 ± 0.5 J/K**.

Table 1
Symbols and definitions used for calorimeter heat-loss characterization.

Symbol	Description
P_{in}	electrical input power supplied by the heating foil to the calorimeter during steady-state tests
$\dot{Q}_{loss}$	heat-flow (loss) rate through the insulation at steady state
ΔT_r	temperature difference between calorimeter interior and ambient
T_{in}	temperature inside the calorimeter, measured by the GTM lid sensor
T_{amb}	ambient temperature outside the calorimeter, measured by the second GTM lid sensor
$G_{emp}(\Delta T_r)$	empirically determined, temperature-dependent effective thermal conductance of the insulated calorimeter
λ	thermal conductivity of the extruded polystyrene insulation
$G_{th\ top}$	theoretical axial thermal conductance through the top insulation segment
$G_{th\ bot}$	theoretical axial thermal conductance through the bottom insulation segment
$G_{th\ side}$	theoretical radial thermal conductance through the cylindrical side insulation
G_{th}	total theoretical thermal conductance of the insulation
L	axial length of the cylindrical sidewall of the insulation
r_1	outer radius of the milling bowl
r_2	inner radius of the surrounding container

To complete the system characterization, the heat capacity contributions of all components are summarized in Table 2 with a total system heat capacity of 678.5 ± 7.0 J/K:

2.3.2.2. Thermal insulation characterization. The heat loss characteristics of the insulated calorimeter system were determined through constant heating experiments at various power levels. A flexible polyimide and etched CuNi44 heating foil, WoF 50060 type B (Winkler GmbH, Heidelberg, Germany) inside the calorimeter bowl provided controlled heat input at eight different power settings ranging from 0.1024 W to 3.0352 W. For each electrical heating rate, the calorimeter reached thermal equilibrium over a continuous electrical heating of 12 h, after which temperature differences between the bowl interior and ambient were recorded for 2.5 h.

At steady state, the electrical input power P_{in} supplied to the calorimeter equals the rate of heat loss $\dot{Q}_{loss}$ through the insulation ($P_{in} = \dot{Q}_{loss}$). The experimental data show a relationship between P_{in} and the resulting temperature difference ΔT_r (where $\Delta T_r = T_{in} - T_{amb}$ represents the temperature difference between the calorimeter interior (T_{in}) and measured ambient (T_{amb}) conditions). For ambient tracking (T_{amb}), the lid was operated outside the mill and the bowl was opened with the sensor exposed to room air. For interior measurements (T_{in}), the lid was mounted on the bowl. From a linear regression of P_{in} versus resulting ΔT_r, the temperature-dependent empirical effective thermal conductance $G_{emp}(\Delta T_r)$ was determined as follows:

$$G_{emp}(\Delta T_r) = 0.35\ \left[mW/K^2\right]{\cdot}\Delta T_r + 54.58\ [mW/K] \quad (1)$$

Additionally, a simplified theoretical estimate of the insulation conductance was derived from the idealized geometry of the milling bowl and surrounding insulation. The total conductance was obtained as the sum of three components: axial heat flow through the top, axial heat flow through the bottom, and radial heat flow through the sidewalls. Only the contribution of the insulation material (extruded polystyrene $\lambda = 0.035\ W/(m{\cdot}K)$ [46])was considered.

Top/bottom were modeled as axial heat flow with [47]:

$$G_{th\ top,bot} = \frac{\lambda \pi r_1^2}{l} \quad (2)$$

$(l_{top} = 25\ mm, l_{bot} = 50\ mm)$

The side was modeled as cylindrical radial conduction with [47]:

$$G_{th\ side} = \frac{2\pi\lambda L}{\ln\left(\frac{r_2}{r_1}\right)}$$

Here L=98 mm is the axial length of the cylindrical sidewall, while $r_1 = 38$ mm is the radius of the milling bowl, $r_2 = 74$ mm the radius of the surrounding container, corresponding to a radial insulation thickness of 36 mm.

Resulting partial theoretical conductances:

$$G_{th\ top} = 6.4\frac{mW}{K}; G_{th\ bot} = 3.2\frac{mW}{K}; G_{th\ side} = 32.3\frac{mW}{K.}$$

Summing up to a total theoretical conductance of:

$$G_{th} = 41.9\ \frac{mW}{K}$$

Assuming homogeneous extruded polystyrene and steady-state con-

Table 2
Heat capacity components of the calorimeter system.

component	heat capacity [J/K]	Method
grinding bowl	592.4 ± 6.8	Experimental
ZrO_2 balls (20)	32.8 ± 1.6	Calculated from material properties
insulation	53.3 ± 0.5	Calculated from material properties
total system	**678.5** ± 7.0	

duction, with no air gaps, negligible contribution from the polypropylene outer layer, and a uniform temperature distribution in the bowl, the empirically determined conductance (which contrary to the simplified theoretical model accounts for temperature difference ΔT_r) is considered more accurate, while the theoretical value confirms the order of magnitude (for realistic ΔT_r of ~10 K) and is expected to only represent an upper limit for the insulation. The empirical conductance calibration implicitly accounts for non-ideal temperature profiles.

2.3.3. Experimental procedure

To ensure reliable and reproducible mechanical-abuse calorimetry, the experimental workflow was conducted according to the defined sequence shown in Fig. 2.

2.3.3.1. Systematic component screening methodology

2.3.3.1.1. Reactivity test. Each chosen material composition is initially subjected to high mechanical energy input to probe its reactivity. Through the milling process, energy is transferred into the calorimeter. Fig. 3 summarizes the reactivity tests by showing pressure (purple) and temperature (orange) as a

function of time during continuous milling. Ignition is defined by a sudden pressure increase (see Fig. 3 c), whose magnitude depends on the composition and sample mass. Note: Due to the limited sampling rate of the grinding-bowl sensor, the absolute maximum cannot be reliably captured and is therefore not suitable as a comparative metric. If no ignition occurs after prolonged milling (see Fig. 3 *a*), the material composition is considered inert. When ignition is detected, the protocol shifts to determining the minimum milling energy required for reliable reaction triggering (E_{mill}).

2.3.3.1.2. Determining the minimum milling energy. Therefore, material compositions are mechanically activated under systematically varied milling conditions. Milling parameters (rotational speed and duration) are initially selected at high energy input and subsequently decreased. After determining the adequate ignition parameters for the chosen material, three calorimetric milling measurements are conducted using previously ignited material (reacted and chemically inactive). E_{mill} therefore represents an operational mechanical reference and does not constitute an independent measurement of the actual mechanical energy dissipation of the unreacted mixture during reaction. The resulting E_{mill}, determined according to the data analysis method, is subtracted from the total calorimetric energy E_{tot} to obtain the net reaction enthalpy E_{net}.

2.3.3.1.3. Calorimetric measurement. The calorimetric measurement follows a three-phase protocol. The temperature and pressure are continuously monitored for the ambient environment as well as for the interior of the grinding bowl throughout all three phases which will be combined to one data set as shown in Fig. 4 *a and b*.

1st Phase - ambient establishment: Thermal equilibration of setup and sample: The sealed grinding bowl containing the materials in the selected composition is allowed to reach a stable initial temperature together with the calorimeter insulation and ambient conditions, defining the reference state prior to the mechanically induced reaction.

2nd Phase - mechanical activation: The milling bowl is transferred from the insulation to the mill, where milling is performed under predetermined conditions. Immediately after milling, the bowl is transferred back to the insulation chamber.

3rd Phase - temperature & pressure monitoring: The calorimeter is kept in the insulation for 2 h while temperature and pressure are monitored over time.

Fig. 4 *a* shows the complete pressure and temperature evolution over all three phases combined for 2 h, while Fig. 4 *b* shows the first 8 min.

2.3.4. Data analysis method

The data analysis method is based on an energy-accounting model; the symbols, variables, and definitions used throughout the following calculations are summarized in Table 3.

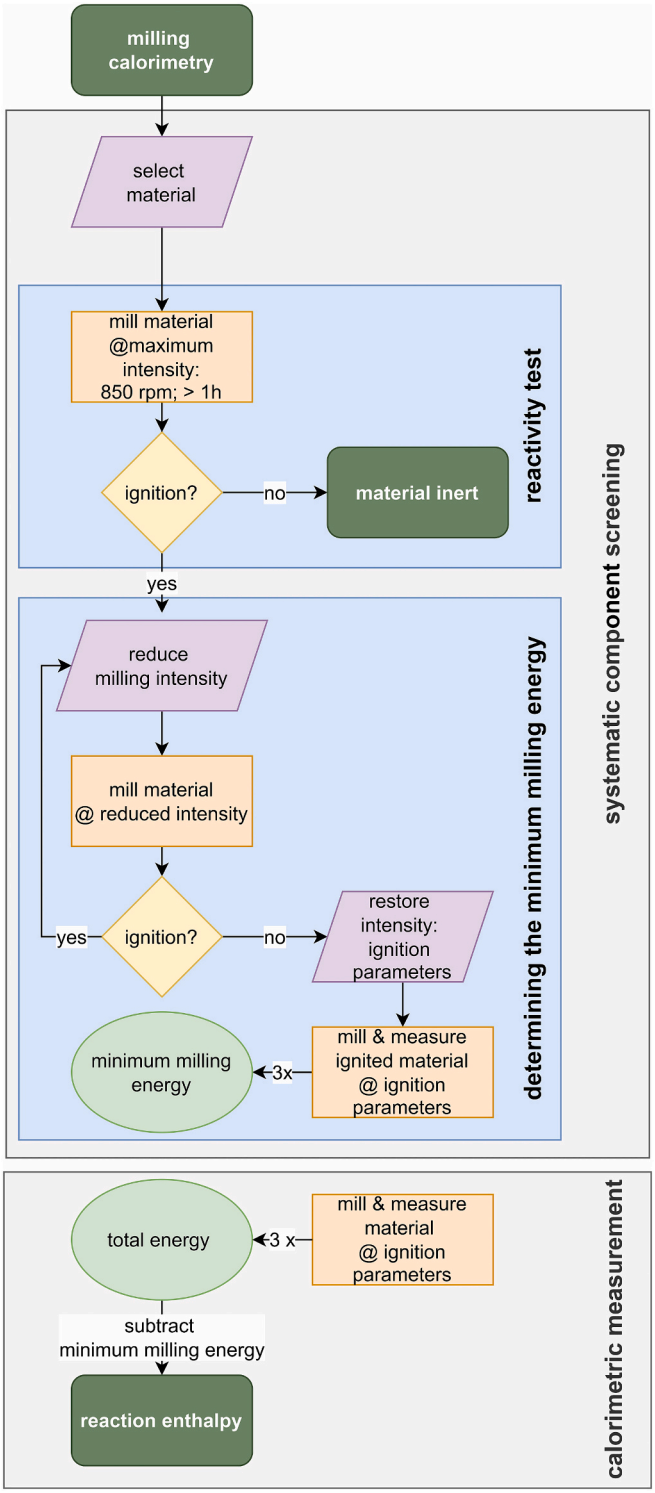


Fig. 2. Experimental procedure flowchart.

For quantifying the energy release of the chosen material composition, the combined experimental data set from the three calorimetric measurement phases mentioned above was processed using a custom Python-based analysis software to ensure consistent and reproducible evaluation across all experiments. To preserve continuity for subsequent time-integration of power to energy, linear interpolation is used for the missing datapoints during transfer. This interpolation is critical for maintaining accuracy in cumulative energy calculations and in Fig. 4 b shown as dotted lines.

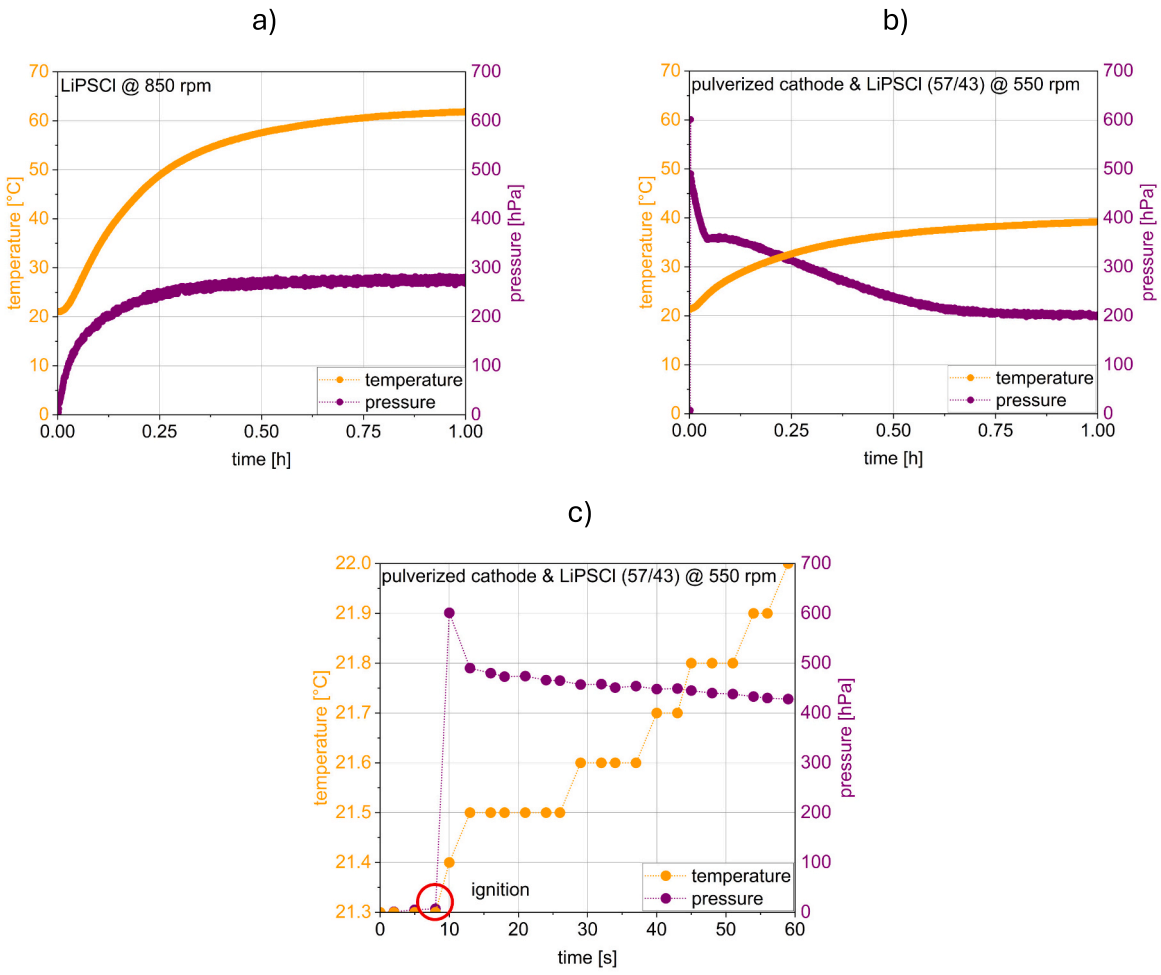


Fig. 3. Reactivity test - pressure (purple) and temperature (orange) during continuous milling over time: (a) Li_6PS_5Cl at 850 rpm (no ignition), 1 h; (b) 57 (wt.) % SOC 100 delithiated $Li_xNi_{0.83}Mn_zCo_{0.17-z}O_2$ ($z < 0.17$) & 43 (wt.) % Li_6PS_5Cl at 550 rpm (ignition), 1 h; (c) same composition, 60 s. (For interpretation of the references to colour in this figure legend, the reader is referred to the web version of this article.)

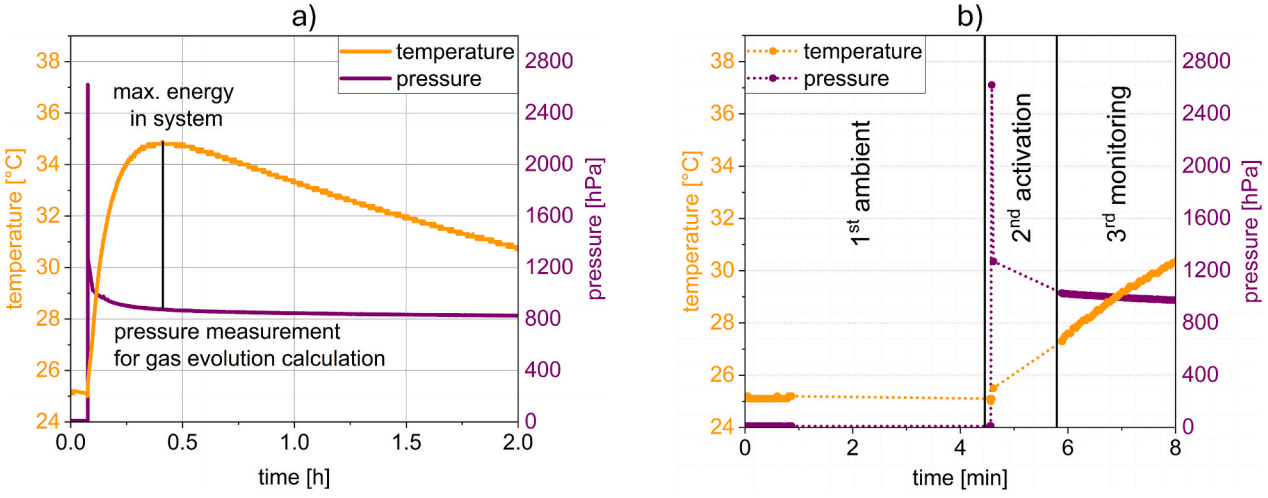


Fig. 4. Mechanical activation of the catholyte (57 (wt.) % SOC 100 delithiated $Li_xNi_{0.83}Mn_zCo_{0.17-z}O_2$ ($z < 0.17$) & 43 (wt.) % Li_6PS_5Cl). Pressure (purple) and temperature (orange) profiles recorded during mechanical-abuse: (a) full experiment over 2 h, including the pressure measurement point used for gas-evolution quantification; (b) first 8 min of the experiment, segmented into the three distinct measurement phases. (For interpretation of the references to colour in this figure legend, the reader is referred to the web version of this article.)

Fig. 5 summarizes this energy-accounting approach by resolving the temperature signal into energy retained in the system (green), energy

Table 3
Symbols and definitions used for energy-accounting model.

Symbol	Description
C_{sys}	total heat capacity of the calorimeter (grinding bowl, balls, insulation) used for energy accounting
T_0	initial start temperature of the calorimeter, defined as the average of the last 20 data points of phase 1 (ambient establishment)
ΔT_s	temperature rise of the calorimeter relative to the Initial start temperature
T_{max}	maximal temperature in the calorimeter
$p_g(T_{max})$	comparable pressure (gauge) at maximal temperature in calorimeter
p_{atm}	atmospheric pressure
t	time variable
$E_{sys}(t)$	thermal energy stored in the calorimeter at time t (green curve)
$\dot{Q}_{loss}(t)$	heat flow rate from the calorimeter to the surroundings (loss) at time t
$E_{loss}(t)$	energy lost to the surroundings up to time t (blue curve)
i	summation index referring to the individual discrete time step
k	upper summation index (total number of discrete time steps)
Δt_i	time interval between two consecutive data points at step i
E_{tot}	total calorimetric energy (red curve)
E_{mill}	minimum milling energy
E_{net}	net energy release
E_{NMC}	net energy normalized per gram of NMC

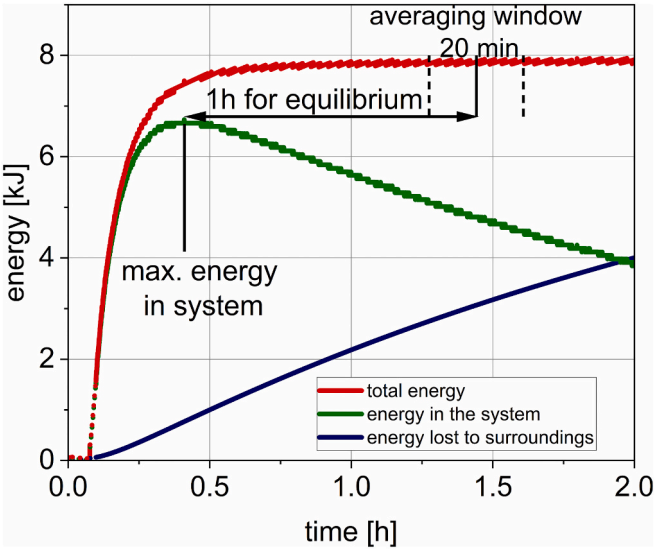


Fig. 5. Energy-accounting model for quantification. Energy in system (green), energy lost to surroundings (blue) and total energy (red)-illustrated for 57/43 (wt./wt.) catholyte composed of 1500 mg shredded NMC cathode (SOC 100) and 970 mg Li_6PS_5Cl. (For interpretation of the references to colour in this figure legend, the reader is referred to the web version of this article.)

lost to the surroundings (blue), and their sum as the total reaction energy (red) as a function of time.

2.3.4.1. Energy in the system - green curve. (Fig. 5): The thermal energy retained in the calorimeter is computed as the product of the calorimeter heat capacity $C_{sys} = 678.5\ J/K$ (Table 2) and the temperature rise relative to the initial start temperature T_0. With $\Delta Ts = T_{in}(t) - T_0$ the energy in the system curve is given by:

$$E_{sys}(t) = \Delta T_s(t) \cdot C_{sys} = energy\ in\ the\ system \tag{3}$$

2.3.4.2. Energy lost to surroundings - blue curve. (Fig. 5). Heat outflow through the insulation is computed from the empirically determined, temperature-dependent loss conductance $G_{emp}(\Delta T_r)$ $[mW/K]$. At each timestamp, the instantaneous heat flow:

$$\dot{Q}_{loss}(t) = G_{emp}(\Delta T_r(t)) \cdot \Delta T_r(t) \tag{4}$$

where ΔT_r is the temperature difference between the calorimeter interior and ambient (at a time t). The cumulative energy dissipated to the surroundings is obtained by time integration,

$$E_{loss}(t) = \int_0^t G_{emp}(\Delta T_r(t)) \cdot \Delta T_r(t) \cdot dt = energy\ lostto\ surroundings \tag{5}$$

and, for the discrete dataset, by numerical summation:

$$E_{loss}(t) = \sum_{i=1}^{k} G_{emp}(\Delta T_{r,i}) \Delta T_{r,i} \Delta t_i = energy\ lost\ to\ surroundings \tag{6}$$

2.3.4.3. Total energy - red curve. (sum of blue and green, Fig. 5) The cumulative reaction energy is the sum of the energy stored in the system and the energy lost to the surroundings. For the discrete dataset:

$$E_{tot}(t) = \Delta T_s(t) \cdot C_{sys} + \sum_{i=1}^{k} G_{emp}(\Delta T_{r,i}) \Delta T_{r,i} \Delta t_i = total\ energy \tag{7}$$

The final determination of total calorimetric energy (E_{tot}) is performed by averaging the total energy curve over a 20-min window (±10 min) centered at 60 min after the temperature maximum is reached (as shown in Fig. 5) This timing represents a balance between allowing sufficient time for thermal acclimatization within the calorimeter assembly and minimizing uncertainties associated with extended extrapolation of heat loss calculations.

Based on these quantities, the net reaction energy was determined as shown in eq. (8). For all mechanical-abuse experiments, the following data analysis procedure was applied to obtain the net energy release of the reaction (E_{net}), the minimum milling energy (E_{mill}) was subtracted from the total calorimetric energy (E_{tot}) and subsequently E_{net} was normalized to the net energy release per gram NMC (E_{NMC}).

$$E_{net} = E_{tot} - E_{mill} \tag{8}$$

The amount of evolved gas was estimated from the pressure-temperature data using the ideal-gas law ($p \bullet V = n \bullet R \bullet T$). As the sensor sampling rate (0.38 Hz) does not reliably capture short-lived, highly dynamic pressure maxima, comparable pressure values were extracted at the temperature maximum (T_{max}) as shown in Fig. 4 a, where thermal equilibrium between competing processes is established: heat transfer from the hot reaction products through the calorimeter (to the sensor) and heat loss through the insulation. The sealed bowl headspace volume was taken as $V = 69.53$ mL (80 mL nominal bowl volume minus 10.47 mL ball volume). Since the GTM sensor reports gauge pressure, pressures were converted to absolute values by adding an atmospheric reference pressure of $p_{atm} = 1013\ hPa$ and referenced to the initial state at T_0. Using temperatures in Kelvin, the evolved gas amount (Δn) was calculated as:

$$\Delta n = \frac{V}{R}\left(\frac{p_g(T_{max}) + p_{atm}}{T_{max}} - \frac{p_{atm}}{T_0}\right) \tag{9}$$

The calculation was automated using Python-based analysis software to ensure consistency across all measurements. A sensitivity analysis assessing the influence of non-ideal gas behavior and the limitations regarding condensable species is provided in the Supporting Information.

All values shown in the results part are reported as mean ± combined standard uncertainty (1σ). Standard deviations (SD) are sample-based. For all calorimeter-mill energies, the combined uncertainty was obtained as the root-sum-of-squares (RSS) of the reproducibility component ($SD/\sqrt{n}$) (with $n = 3$) and the method uncertainty from validation (MAPE · mean(E)). For E_{net}, combined standard uncertainty of E_{mill} (Table S 2) was additionally propagated by RSS.

2.3.5. Method validation

This section addresses the validation of the calorimeter-mill by demonstrating internal consistency of the energy-accounting model as well as reporting its quantitative accuracy under controlled conditions using an independent energy reference.

As an internal consistency check of the energy-accounting framework, the total energy curve becomes essentially constant over time (see red curve in Fig. 5), demonstrating that the calculated energy lost to the surroundings (blue curve) accurately complements the energy retained in the system (green curve). This stable plateau provides an internal logic check for the determined heat-capacity and thermal-conductance parameters. To complement this with an external independent reference, quantitative systematic validation experiments were performed using controlled electrical heating to assess the accuracy of the complete calorimeter, including all component contributions. Two series of heating experiments were conducted in triplicate: one without grinding balls (calorimeter heat capacity: 645.7 J/K) and one with grinding balls (calorimeter heat capacity: 678.5 J/K) see Table 2.

An electric heating foil (flexible polyimide and etched CuNi44 heating foil, WoF 50,060 type B (Winkler GmbH, Heidelberg, Germany) was adhered to the inner wall of the calorimeter, with electrical connections routed through a prepared sealing gasket. Energy input was measured using a four-wire configuration to eliminate cable resistance effects, with current measured via a precision shunt resistor. The electrical energy ($E = U \bullet I \bullet t$) was compared to the calorimetrically determined energy calculated by the data analysis method described above. The data is listed in Table 4.

The validation results demonstrate close agreement between the electrically and calorimetrically determined energy: Across all validation experiments, a mean absolute percentage error (MAPE) of 0.77% was obtained, with a sample-based standard deviation of 0.44%, reflecting the reproducibility of the energy-accounting model. The reported MAPE therefore describes the validated accuracy of E_{tot} and does not include milling-specific systematic uncertainties such as transfer heat loss or the mechanical milling correction.

To define a conservative accuracy limit, an upper estimate of the relative error was calculated as MAPE $+1.96 \cdot$SD $= 1.63\%$. For a representative validation energy of 6.46 kJ, corresponding to the mean electrical energy input of the validation experiments summarized in Table 4, this corresponds to an absolute error of approximately 105 J. Assuming that this absolute error is approximately constant over the relevant operating range of the calorimeter, as the dominant uncertainty contributions are governed by fixed system properties such as heat capacity, sensor resolution, and the calibrated heat-loss model, the relative uncertainty decreases with increasing released energy. Under this assumption, adopting a conservative target accuracy criterion of $\leq$2% relative error based on this conservative estimate, this condition is achieved for total calorimetric energies $E_{tot} \geq 5.3$ kJ.

3. Results

3.1. Systematic component screening of shredded cathode and Li_6PS_5Cl

To systematically evaluate the reactivity between sulfide-based solid electrolyte and delithiated cathode material under mechanical-abuse conditions, a hierarchical screening approach (as described in the experimental procedure (see Fig. 2) was implemented. The specific compositions including shredded cathode material and Li_6PS_5Cl were selected based on automotive-industry-relevant cell designs. [15,48]

Four material compositions were investigated:

- 100 (wt.) % SOC 100 delithiated $Li_xNi_{0.83}Mn_zCo_{0.17-z}O2$ ($z < 0.17$) **shredded cathode material** *
- 78 (wt.) % SOC 100 delithiated $Li_xNi_{0.83}Mn_zCo_{0.17-z}O_2$ ($z < 0.17$) & 22 (wt.) % Li_6PS_5Cl (**78/22 catholyte**)*
- 57 (wt.) % SOC 100 delithiated $Li_xNi_{0.83}Mn_zCo_{0.17-z}O_2$ ($z < 0.17$) & 43 (wt.) % Li_6PS_5Cl (**57/43 catholyte**)*
- 100 (wt.) % **Li_6PS_5Cl** solid electrolyte

*The weight ratios show the calculated ratios between NMC (in uncharged, lithiated state (x = 1)) and Li_6PS_5Cl. However, Aluminum current-collector, binder and conductive carbon were present in the material compositions.

3.1.1. Reactivity test of shredded cathode and Li_6PS_5Cl

The reactivity of the material compositions was tested as described in the experimental procedure: Fig. 3 a shows exemplary milling of pure Li_6PS_5Cl at 850 rpm for 1 h, where no ignition is observed, whereas Fig. 3 *b* and *3 c* show the 57/43 catholyte milled at 550 rpm, exhibiting a distinct ignition event within the first 15 s. All cathode material-containing samples exhibited such an ignition event.

3.1.2. Determining minimum milling energy

The reactivity test is followed by determining the minimum milling energy from previously ignited (inert) cathode material, yielding values of 3303 $\pm$ 91 J for the high-energy ignition parameters necessary for pure shredded cathode material and 359 $\pm$ 7 J for the standard ignition parameters for the compositions:

- high-energy ignition parameters (60 s at 850 rpm, for pure shredded cathode material) and
- standard ignition parameters (15 s at 550 rpm, for the catholyte compositions).

The minimum milling energy (E_{mill}) and ignition events are listed in Table 5.

These operational mechanical reference energies were subsequently subtracted from all reaction measurements, using the data analysis method, to obtain the net chemical energy release E_{net}. Relative to the total calorimetric energy E_{tot}, the mechanical correction E_{mill} accounts for 47.4% for the shredded cathode, 5.4% for the 78/22 catholyte, and 4.6% for the 57/43 catholyte. As an additional control, 1500 mg of pure Li_6PS_5Cl was milled in triplicate for 60 s at 850 rpm, with no ignition observed. The measured energies were 3348, 3236, and 3222 J, yielding a mean of 3269 $\pm$ 47 J (combined standard uncertainty, 1σ, calculated as described in Section 2.3.4). This differs by 1.0% from the operational mechanical reference of 3303 $\pm$ 91 J determined using previously reacted cathode material under identical milling parameters. The close agreement supports the use of this operational reference under the investigated conditions, while not establishing identical mechanical dissipation in the unreacted mixture during reaction.

3.1.3. Calorimetrically determined energy

The samples with mass fractions listed in Table 6 were measured as described and showed similar pressure and temperature profiles. As an

Table 4
Validation results for the calorimeter.

configuration	trial	calorimetric E_{tot} [J]	electrical energy [J]	error [%]
Without balls	1	6326.7	6360.0	0.52
(645.7 J/K)	2	6350.2	6416.2	1.03
	3	6444.8	6409.3	0.55
With balls	4	6549.5	6534.3	0.23
(678.5 J/K)	5	6476.4	6531.1	0.84
	6	6409.5	6505.0	1.47
	MAPE			0.77

Table 5
Milling ignition parameters and minimum operational mechanical energy input for reliable ignition.

	milling ignition parameters	E_{mill} [J] ($n = 3$)	ignition
shredded cathode	60 s, 850 rpm	3303 $\pm$ 91	yes
78/22 catholyte	15 s, 550 rpm	359 $\pm$ 7	yes
57/43 catholyte	15 s, 550 rpm	359 $\pm$ 7	yes
Li_6PS_5Cl	up to 5 h, 850 rpm	–	no

Table 6
Experimental composition, calorimetric energies, comparable pressures and gas evolution.

	shredded cathode (n = 3)	78/22 catholyte (n = 3)	57/43 catholyte (n = 3)
shredded cathode [mg]	1500	1500	1500
NMC [mg]	1311	1311	1311
Li_6PS_5Cl [mg]	0	364	970
E_{net} [J]	3669 ± 208	6281 ± 211	7437 ± 164
E_{NMC} [$J/g_{(NMC)}$]	2799 ± 159	4791 ± 161	5673 ± 125
$p(T_{max})$ [hPa] (gauge)	1815 ± 44	1503 ± 20	889 ± 24
gas evolution at T_{max} [mmol]	4.9 ± 0.13	4.0 ± 0.06	2.3 ± 0.06

example, the experiment with the 57/43 catholyte composition shown in Fig. 4 a is described:

Temperature evolution: Following ignition, the lid-sensor temperature increased from 25.0 °C (T_0; initial room temperature) to 34.9 °C at T_{max} ($\Delta T \approx 9.9$ °C). Here, T_{max} was reached with a pronounced delay (~25 min) after the initial ignition event. Pressure evolution: Ignition is accompanied by an immediate pressure increase followed by a strong decline to an elevated plateau (Fig. 4 a), consistent with rapid gas evolution followed by cooling and continuous heat dissipation from the system. Reaction completeness: For all investigated material compositions, pressure monitoring during prolonged milling of the reacted compositions (>1 h) showed no additional pressure spikes beyond the initial ignition event, (see Fig. 3 b). Overall, the shared trace morphology across all igniting compositions indicates that the key differences are reflected in the quantitative metrics summarized in Table 6 as average (n = 3): The pure shredded cathode material released 3669 ± 208 J (corresponding to 2799 ± 159 $J/g_{(NMC)}$, normalized to NMC), accompanied by a representative pressure of 1815 ± 44 hPa (at T_{max}) and a gas evolution of 4.9 ± 0.13 mmol at T_{max}. The 78/22 catholyte composition showed a higher net energy release of 6281 ± 211 J (4791 ± 161 $J/g_{(NMC)}$), while the comparable pressure and gas evolution decreased to 1503 ± 20 hPa and 4.0 ± 0.06 mmol, respectively. The 57/43 catholyte composition released 7437 ± 164 J net energy (5673 ± 125 $J/g_{(NMC)}$), despite a further reduction in comparable pressure (889 ± 24 hPa) and gas generation (2.3 ± 0.06 mmol).

3.2. Differential scanning calorimetry reference

To establish a thermal reference context to the mechanically induced energy release, differential scanning calorimetry was performed in triplicate on a material composition corresponding to the 57/43 catholyte. The measurements yielded an integrated heat release normalized to the mass of NMC ($E_{DSC(NMC)}$) of 3724 ± 236 $J/g_{(NMC)}$ up to 550 °C (n = 3). Three reproducible exothermic features were observed, which define three temperature regions (shown in Fig. 6) at approximately 215–230 °C (yellow), 260–340 °C (red), and 470–510 °C (green). These data define the thermal reference for contextualizing the mechanically induced energy release discussed below.

4. Discussion

The following discussion addresses the origin of the observed energy release under mechanical activation and places the results within the context of worst-case safety assessment.

A clear and expected discrepancy is observed between the energy release measured by the calorimeter-mill and by DSC, with the 57/43 catholyte yielding 3724 ± 236 $J/g_{(NMC)}$ in DSC compared to 5673 ± 125 $J/g_{(NMC)}$ under mechanical activation. This discrepancy may arise from three principal methodological differences.

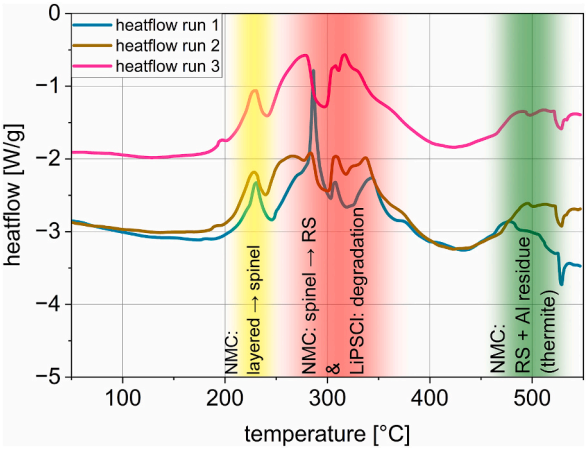


Fig. 6. Differential scanning calorimetry (DSC) heat-flow profiles of a 57/43 (wt./wt.) catholyte composition (excluding Aluminum current collector) measured at a heating rate of 5 K/min up to 550 °C.

(i) In the calorimeter-mill, reactions are initiated by mechanical activation, such that multiple processes can occur near-simultaneously, in contrast, DSC probes thermally triggered processes sequentially with rising temperature, which can lead to different pathways with different reaction enthalpies.

(ii) The DSC protocol is limited to an upper temperature of 550 °C and therefore cannot capture phenomena that may occur at higher temperatures. Mechanical impacts can locally generate short-lived hotspots, enabling additional reactions between released oxygen species and Li_6PS_5Cl or its decomposition products.

(iii) A systematic difference arises from the DSC system boundary. In the present DSC experiments, the aluminum current collector was excluded to obtain sufficiently homogeneous samples at the small sample masses used. Previous DSC/TG-DSC studies have demonstrated that current-collector-containing NMC electrodes can be investigated thermally and that reactions involving the aluminum current collector can contribute substantially to the measured heat release [49]. The cathode material was therefore removed from the aluminum foil and mixed with Li_6PS_5Cl; while visible aluminum fragments were removed as thoroughly as possible, it remains plausible that small amounts of aluminum from the current collector were still present in the DSC samples.

While points (i) and (ii) mainly limit the direct comparability of mechanical and thermal activation, point (iii) is critical because it determines whether reactions involving the current collector are included. Accordingly, the DSC measurements are used here as a thermal reference rather than as a direct quantitative method-to-method comparison with the calorimeter-mill. The DSC trace (Fig. 6) shows three temperature regions at approximately 215–230 °C (yellow), 260–340 °C (red), and 470–510 °C (green).

The first temperature region (215–230 °C) corresponds [2,20,50,51] to the onset of structural instability of the highly delithiated NMC cathode and the beginning of lattice-oxygen release [52], representing an intrinsic exothermic contribution of the cathode material.

The second temperature region (260–340 °C) is associated with continued oxygen release and progressive structural degradation toward rock-salt (RS) like phases [52], accompanied by increased reactivity of the decomposition products; in this region, multiple partially uncharacterized reactions may overlap and compete, making variations in the exothermic signal plausible.

The third temperature region (470–510 °C) likely reflects advanced cathode decomposition [52] and, where aluminum is present,

can include additional exothermic contributions from current-collector-coupled thermite reactions [53]. In this context, the small exotherm around ~490 °C in the DSC trace is consistent with the possible presence of trace amounts of aluminum originating from the current collector. Previous DSC studies have shown that fully charged NMC cathodes can exhibit an additional exothermic contribution [25], depending on cathode composition and experimental configuration at elevated temperatures when aluminum is present, with reported onset temperatures of above 480 °C for NMC111. In the calorimeter-mill experiments, the current collector is retained by design and can therefore participate in such high-temperature reactions [25], resulting in a more system-relevant boundary for worst-case assessment.

Mechanically induced reactions between delithiated NMC and sulfide solid electrolytes have been demonstrated previously, including ignition during mechanical mixing and grinding [32,34]. These studies established the pronounced reactivity of delithiated NMC/sulfide systems and provided detailed insight into the associated reaction chemistry [20]. While exothermic decomposition of delithiated NMC cathodes has been mentioned through DSC measurements [54–56], to the authors' knowledge, this represents the first quantitative calorimetric assessment of mechanically-induced decomposition of delithiated NMC. Using the described energy-accounting approach, the delithiated NMC cathode material including the current collector released 2799 ± 159 J/g(NMC), accompanied by a gas evolution of 4.9 ± 0.1 mmol.

The normalized energy release increases systematically from the shredded cathode (2799 $J/g_{(NMC)}$) to the 78/22 catholyte (4791 $J/g_{(NMC)}$) and further to the 57/43 catholyte (5673 $J/g_{(NMC)}$), indicating that the presence of Li_6PS_5Cl enhances the exothermic response. Additionally, catholyte compositions containing Li_6PS_5Cl ignite at substantially lower mechanical activation energies than the shredded cathode alone. This behavior, together with the DSC profiles, indicates the contribution of two coupled processes: intrinsic decomposition of the delithiated cathode material as a primary driver of thermal runaway [33,57] and additional exothermic interactions involving the solid electrolyte, its decomposition products or other components such as current collector, binder and conductive carbon.

The inverse relationship between energy release and gas evolution, with pressure decreasing from 1815 hPa for the shredded cathode to 889 hPa for the 57/43 catholyte, together with the DSC-derived temperature regions and the known NMC phase transition associated with lattice-oxygen release at ~230 °C, provides insight into the underlying reaction mechanisms.

High gas generation for the shredded cathode is consistent with oxygen evolution, whereas the reduced gas evolution together with increased heat release upon Li_6PS_5Cl addition could be consistent with partial consumption of oxygen species in secondary exothermic reactions with the sulfide electrolyte. However, this interpretation remains speculative without direct gas-species or post-reaction chemical analysis.

Taken together, the difference in measured energies between the calorimeter-mill and DSC reflects the combined effects of different activation conditions, sample compositions, and experimental system boundaries. The higher value measured in the calorimeter-mill may arise from (i) simultaneous and competing mechanically triggered reactions, (ii) hotspot-driven pathways beyond the DSC temperature limit, and (iii) a different system boundary due to exclusion of the aluminum current collector; combined with the composition-dependent increase in heat release and the inverse trend between heat release and gas evolution, these findings show that mechanical activation constitutes a complementary mechanical-abuse approach to conventional thermally driven DSC testing, positioning the calorimeter-mill methodology as a quantitative mechanical-abuse method for probing worst-case energy release. The method requires reactions to be exothermic, triggerable and completed within short milling durations. The uncertainty associated with the operational E_{mill} baseline becomes particularly relevant for systems requiring a high operational mechanical energy input, and further refinement of the mechanical energy accounting should therefore be addressed in future work. The ~15-s transfer time between mill and insulation chamber (after ignition) results in a small unaccounted energy loss. While this loss is minimized through rapid transfer and remains small due to the system's thermal inertia, it precludes quantitative assessment of slow exothermic processes that develop over extended periods. Additionally, the method's accuracy benefits from larger sample energies which generate greater temperature differences and thus improved signal-to-noise ratios, though this requirement may limit applicability for expensive or scarce materials. The GTM bowl's operational limits (2 MPa, 110 °C maximum) define the upper boundary for safely measurable reaction intensities.

5. Conclusion

This work presents a calorimeter-mill methodology for quantitative material-level safety screening of all-solid-state battery (ASSB) materials under extreme mechanical activation, with the aim of assessing their energy-release potential under defined conditions. The approach couples planetary ball milling with calorimetry and in situ pressure/temperature monitoring in a sealed grinding bowl. Mechanical milling enforces intimate interfacial contact and continuous renewal of reactive surfaces, while the calorimetric evaluation quantifies the net chemical energy release by correcting the total calorimetric energy for the operational mechanical reference E_{mill}. To enable this correction, the system was characterized by determining the effective heat capacity of the complete calorimeter assembly (bowl, grinding balls, insulation) and by experimentally calibrating heat losses through the insulation as a temperature-dependent effective conductance. An energy-accounting model resolves energy retained in the calorimeter and cumulative energy lost to the surroundings, whose sum yields the total calorimetric energy. The calorimetric energy-accounting model was validated using controlled electrical heating, demonstrating high accuracy and reproducibility (MAPE <1%), thereby providing a robust quantitative basis for early-stage safety screening and go/no-go decisions prior to cell-level fabrication.

The method was demonstrated on cathode-relevant sulfide-based ASSB material sets comprising delithiated Ni-rich NMC (SOC 100 (4.2 V)) in electrode form (including binder, conductive carbon, and aluminum current-collector) and different compositions with Li_6PS_5Cl. Pressure monitoring served as the primary real-time indicator for ignition, capturing rapid reaction onset that precedes the delayed temperature maximum caused by the thermal mass and sensor location. Shredded cathode material (including aluminum current collector) underwent rapid, exothermic decomposition under mechanical activation, releasing 2799 ± 159 $J/g_{(NMC)}$ and generating 4.9 ± 0.1 mmol gas at T_{max}. Incorporation of Li_6PS_5Cl increased the normalized energy release systematically up to 5673 ± 125 $J/g_{(NMC)}$ for a 57/43 catholyte composition, while simultaneously reducing gas evolution to 2.3 ± 0.1 mmol. The inverse trend between released heat and gas formation is compatible with secondary exothermic pathways that may involve consumption of oxygen species provided by the NMC; however, this interpretation cannot be confirmed without direct gas-species or post-reaction chemical analysis.

To contextualize the mechanically induced energy release, differential scanning calorimetry was performed on a corresponding catholyte composition (without deliberate inclusion of visible aluminum fragments) up to 550 °C, yielding 3724 ± 236 $J/g_{(NMC)}$ and three reproducible exothermic regions.

Overall, the calorimeter-mill should therefore be considered a complementary material-level worst-case screening approach rather than a representation of a specific cell-level mechanical-abuse event. The pronounced composition dependence observed in this study highlights the importance of considering interactions between electrode and solid-electrolyte components when assessing the energetic hazard of ASSB

material combinations. Future work should extend the methodology to further cathode and solid-electrolyte chemistries and establish how the determined material-level energy-release boundaries relate to standardized cell-level abuse tests.

CRediT authorship contribution statement

Florian Salk: Writing – review & editing, Writing – original draft, Visualization, Validation, Project administration, Methodology, Investigation, Formal analysis. **Thomas Bayha:** Writing – review & editing, Validation, Project administration, Methodology, Conceptualization. **Sebastian Scharner:** Writing – review & editing, Supervision, Resources, Project administration, Conceptualization. **Philipp Heugel:** Writing – review & editing, Supervision, Project administration. **Martin Miller:** Writing – review & editing, Validation, Methodology. **Thomas Berger:** Writing – review & editing, Project administration, Conceptualization. **Franziska Klein:** Writing – review & editing, Supervision, Project administration. **Jens Tübke:** Writing – review & editing, Supervision, Resources.

Declaration of Generative AI and AI-assisted technologies in the writing process

During the preparation of this work, the authors used ChatGPT, Anthropic Claude, and Google NotebookLM to support literature search, source identification, information retrieval from literature, language editing, text structuring, and manuscript preparation. After using these tools, the authors reviewed and edited the content as needed and take full responsibility for the content of the publication.

Funding

Parts of this work were funded and financially supported by Bayerische Motoren Werke Aktiengesellschaft (BMW AG). The support consisted of material costs and personnel time. BMW AG also provided chemicals and samples used in this study. Parts of this work were also funded by the German Federal Ministry of Research, Technology and Space (BMFTR; formerly BMBF) and the New Energy and Industrial Technology Development Organization (NEDO) within the German–Japanese research project “BeSafe” (grant no. 03XP0592A). The support consisted of material and personnel costs.

Declaration of competing interest

The authors declare the following financial interests/personal relationships which may be considered as potential competing interests: Florian Salk reports financial support was provided by Bayerische Motoren Werke Aktiengesellschaft (BMW AG). Sebastian Scharner reports a relationship with Bayerische Motoren Werke Aktiengesellschaft (BMW AG) that includes: employment. If there are other authors, they declare that they have no known competing financial interests or personal relationships that could have appeared to influence the work reported in this paper.

Acknowledgements

The authors thank Sebastian Schuhmann for discussions and support; Heike Schuppler for carrying out DSC measurements; Michael Holzapfel for advice and discussions; Sebastian Geiger for technical support and discussions; Jan Petit for support with the glovebox; Patrik Fanz for discussions and construction support; Johannes Sicklinger for structural support and coordination; Patrick Walke for discussions; Peer Bärmann for the organization of materials; Michael Abert for discussions and advice; Paul Müller for project work and enabling the idea; Fritz Bruch for discussions and support; Kevin Gneupel for discussions and support; Niklas Röttgen for discussions and glovebox support; Franziska Schneider for structural support and discussions; and Stefanie Mutterer for reviewing the manuscript.

Appendix A. Supplementary data

Supplementary data to this article can be found online at https://doi.org/10.1016/j.est.2026.125365.

Data availability

The authors do not have permission to share data.

References

[1] S. Wang, Y. Wu, T. Ma, L. Chen, H. Li, F. Wu, Thermal stability between Sulfide solid electrolytes and oxide cathode, ACS Nano 16 (2022) 16158–16176, https://doi.org/10.1021/acsnano.2c04905.
[2] Y. Li, X. Liu, L. Wang, X. Feng, D. Ren, Y. Wu, G. Xu, L. Lu, J. Hou, W. Zhang, Y. Wang, W. Xu, Y. Ren, Z. Wang, J. Huang, X. Meng, X. Han, H. Wang, X. He, Z. Chen, K. Amine, M. Ouyang, Thermal runaway mechanism of lithium-ion battery with $LiNi_{0.8}Mn_{0.1}Co_{0.1}O_2$ cathode materials, Nano Energy 85 (2021) 105878, https://doi.org/10.1016/j.nanoen.2021.105878.
[3] G. Wang, X. Guo, J. Chen, P. Han, Q. Su, M. Guo, B. Wang, H. Song, Safety performance and failure criteria of Lithium-ion batteries under mechanical abuse, Energies 16 (2023) 6346, https://doi.org/10.3390/en16176346.
[4] Y. He, J. Wang, C. Rong, W. Li, Z. Gao, D. Wang, Y. Chen, Status of cell-level thermal safety assessments toward optimization of all-solid-state batteries, Cell Rep. Phys. Sci. 5 (2024) 102056, https://doi.org/10.1016/j.xcrp.2024.102056.
[5] N. Vujnović, K. Hohenberg, P. Höschele, J. Moser, C. Ellersdorfer, A comprehensive review of thermal runaway and thermal runaway propagation modelling approaches in lithium-ion batteries, J. Energy Storage 139 (2025) 118685, https://doi.org/10.1016/j.est.2025.118685.
[6] X. Lai, J. Yao, C. Jin, X. Feng, H. Wang, C. Xu, Y. Zheng, A review of Lithium-ion battery failure hazards: Test standards, accident analysis, and safety suggestions, Batteries 8 (2022) 248, https://doi.org/10.3390/batteries8110248.
[7] United Nations, Manual of Tests and Criteria - Eighth Revised Edition: UN 38.3, United Nations, New York, 2023 accessed 27 October 2025.
[8] International Electrotechnical Commission, Secondary Cells and Batteries Containing Alkaline or Other Non-acid Electrolytes – Safety Requirements for Portable Sealed Secondary Cells, and for Batteries Made from them, for Use in Portable Applications: - Part 2: Lithium Systems, IEC, Geneva, Switzerland, 2021.
[9] SAE International, SAE J 2464:2021-08-23: Electric and Hybrid Electric Vehicle Rechargeable Energy Storage System (RESS) Safety and Abuse Testing, SAE International, 400 Commonwealth Drive, Warrendale, PA, United States, 2021. https://www.dinmedia.de/en/standard/sae-j-2464/345426399. accessed 1 June 2026.
[10] China National Standards, Electric vehicles traction battery safety requirements: GB 38031-2025, China National Standards, 2025. https://www.gbstandards.org/.
[11] Automotive Research Association of India, AIS-156: amendments 1–4, Ministry of Road Transport and Highways (MoRTH), 2023. https://hmr.araiindia.com/.
[12] D. Ren, L. Lu, R. Hua, G. Zhu, X. Liu, Y. Mao, X. Rui, S. Wang, B. Zhao, H. Cui, M. Yang, H. Shen, C.-Z. Zhao, L. Wang, X. He, S. Liu, Y. Hou, T. Tan, P. wang, Y. Nitta, M. Ouyang, Challenges and opportunities of practical sulfide-based all-solid-state batteries, eTransportation 18 (2023) 100272, https://doi.org/10.1016/j.etran.2023.100272.
[13] T. Schmaltz, F. Hartmann, T. Wicke, L. Weymann, C. Neef, J. Janek, A roadmap for solid-state batteries, Adv. Energy Mater. 13 (2023) 2301886, https://doi.org/10.1002/aenm.202301886.
[14] J. Janek, W.G. Zeier, Challenges in speeding up solid-state battery development, Nat. Energy 8 (2023) 230–240, https://doi.org/10.1038/s41560-023-01208-9.
[15] J. Kim, M.J. Kim, J. Kim, J.W. Lee, J. Park, S.E. Wang, S. Lee, Y.C. Kang, U. Paik, D. S. Jung, T. Song, High-performance all-solid-state batteries enabled by intimate interfacial contact between the cathode and Sulfide-based solid electrolytes, Adv. Funct. Mater. 33 (2023) 2211355, https://doi.org/10.1002/adfm.202211355.
[16] T. Schmaltz, T. Wicke, L. Weymann, P. Voß, C. Neef, A. Thielmann, Solid-State Battery Roadmap 2035+, Fraunhofer-Institut für System- und Innovationsforschung ISI, Karlsruhe, 2022.
[17] F. Thomas, L. Mahdi, J. Lemaire, D.M.F. Santos, Technological advances and market developments of solid-state batteries: A review, Materials 17 (2024) 239, https://doi.org/10.3390/ma17010239.
[18] N. Johnson, P. Albertus, Modeling thermal behavior and safety of large format all-solid-state lithium metal batteries under thermal ramp and short circuit conditions, J. Electrochem. Soc. 169 (2022) 60546, https://doi.org/10.1149/1945-7111/ac79cf.
[19] A.M. Bates, Y. Preger, L. Torres-Castro, K.L. Harrison, S.J. Harris, J. Hewson, Are solid-state batteries safer than lithium-ion batteries? Joule 6 (2022) 742–755, https://doi.org/10.1016/j.joule.2022.02.007.
[20] X. Rui, D. Ren, X. Liu, X. Wang, K. Wang, Y. Lu, L. Li, P. Wang, G. Zhu, Y. Mao, X. Feng, L. Lu, H. Wang, M. Ouyang, Distinct thermal runaway mechanisms of sulfide-based all-solid-state batteries, Energy Environ. Sci. (2023), https://doi.org/10.1039/D3EE00084B.

[21] Y. Ren, T. Danner, A. Moy, M. Finsterbusch, T. Hamann, J. Dippell, T. Fuchs, M. Müller, R. Hoft, A. Weber, L.A. Curtiss, P. Zapol, M. Klenk, A.T. Ngo, P. Barai, B. C. Wood, R. Shi, L.F. Wan, T.W. Heo, M. Engels, J. Nanda, F.H. Richter, A. Latz, V. Srinivasan, J. Janek, J. Sakamoto, E.D. Wachsman, D. Fattakhova-Rohlfing, Oxide-based solid-state batteries: A perspective on composite cathode architecture, Adv. Energy Mater. 13 (2023) 2201939, https://doi.org/10.1002/aenm.202201939.

[22] Y. Guo, S. Wu, Y.-B. He, F. Kang, L. Chen, H. Li, Q.-H. Yang, Solid-state lithium batteries: Safety and prospects, eScience 2 (2022) 138–163, https://doi.org/10.1016/j.esci.2022.02.008.

[23] Y. Wu, J. Xu, P. Lu, J. Lu, L. Gan, S. Wang, R. Xiao, H. Li, L. Chen, F. Wu, Thermal stability of sulfide solid electrolyte with lithium metal, Adv. Energy Mater. 13 (2023) 2301336, https://doi.org/10.1002/aenm.202301336.

[24] S.-J. Yang, J.-K. Hu, F.-N. Jiang, X.-B. Cheng, S. Sun, H.-J. Hsu, D. Ren, C.-Z. Zhao, H. Yuan, M. Ouyang, L.-Z. Fan, J.-Q. Huang, Q. Zhang, Oxygen-induced thermal runaway mechanisms of Ah-level solid-state lithium metal pouch cells, eTransportation 18 (2023) 100279, https://doi.org/10.1016/j.etran.2023.100279.

[25] T. Inoue, K. Mukai, Are all-solid-state Lithium-ion batteries really safe?-verification by differential scanning calorimetry with an all-inclusive microcell, ACS Appl. Mater. Interfaces 9 (2017) 1507–1515, https://doi.org/10.1021/acsami.6b13224.

[26] C. Capiglia, J. Yang, N. Imanishi, A. Hirano, Y. Takeda, O. Yamamoto, DSC study on the thermal stability of solid polymer electrolyte cells, J. Power Sources 119-121 (2003) 826–832, https://doi.org/10.1016/S0378-7753(03)00280-5.

[27] D. Ren, X. Liu, X. Feng, L. Lu, M. Ouyang, J. Li, X. He, Model-based thermal runaway prediction of lithium-ion batteries from kinetics analysis of cell components, Appl. Energy 228 (2018) 633–644, https://doi.org/10.1016/j.apenergy.2018.06.126.

[28] A. Atarashi, H. Tsukasaki, M. Otoyama, H. Kowada, S. Mori, A. Hayashi, M. Tatsumisago, Ex situ investigation of exothermal behavior and structural changes of the Li_3PS_4- $LiNi_{1/3}Mn_{1/3}Co_{1/3}O2$ electrode composites, Solid State Ionics 342 (2019) 115046, https://doi.org/10.1016/j.ssi.2019.115046.

[29] H. Tsukasaki, T. Uchiyama, K. Yamamoto, S. Mori, Y. Uchimoto, H. Kowada, A. Hayashi, M. Tatsumisago, Exothermal mechanisms in the charged $LiNi_{1/3}Mn_{1/3}Co_{1/3}O2$ electrode layers for sulfide-based all-solid-state lithium batteries, J. Power Sources 434 (2019) 226714, https://doi.org/10.1016/j.jpowsour.2019.226714.

[30] S.-K. Jung, H. Gwon, S.-S. Lee, H. Kim, J.C. Lee, J.G. Chung, S.Y. Park, Y. Aihara, D. Im, Understanding the effects of chemical reactions at the cathode–electrolyte interface in sulfide based all-solid-state batteries, J. Mater. Chem. A 7 (2019) 22967–22976, https://doi.org/10.1039/c9ta08517c.

[31] H. Tsukasaki, M. Otoyama, Y. Mori, S. Mori, H. Morimoto, A. Hayashi, M. Tatsumisago, Analysis of structural and thermal stability in the positive electrode for sulfide-based all-solid-state lithium batteries, J. Power Sources 367 (2017) 42–48, https://doi.org/10.1016/j.jpowsour.2017.09.031.

[32] T. Kim, H. Chang, G. Song, S. Lee, K. Kim, S. Lee, J. Moon, K.T. Lee, Critical factors contributing to the thermal runaway of thiophosphate solid electrolytes for all-solid-state batteries, Adv. Funct. Mater. 34 (2024) 2404806, https://doi.org/10.1002/adfm.202404806.

[33] T. Kim, K. Kim, S. Lee, G. Song, M.S. Jung, K.T. Lee, Thermal runaway behavior of Li_6PS_5Cl solid electrolytes for $LiNi_{0.8}Co_{0.1}Mn_{0.1}O2$ and $LiFePO_4$ in all-solid-state batteries, Chem. Mater. 34 (2022) 9159–9171, https://doi.org/10.1021/acs.chemmater.2c02106.

[34] Y. Wu, S. Zhang, Y. Sun, L. Huang, J. Xu, C. Liu, S. Zhu, Z. Jiang, T. Gong, L. Guo, L. Cui, T. Liu, J. Ju, G. Cui, Electrochemical initiation and chemical reaction cascades in dual-stage thermal runaway in sulfide-based all-solid-state batteries, Nat. Commun. 17 (2026), https://doi.org/10.1038/s41467-026-69472-3.

[35] L. Yiding, W. Wenwei, L. Cheng, Y. Xiaoguang, Z. Fenghao, Multi-physics safety model based on structure damage for lithium-ion battery under mechanical abuse, J. Clean. Prod. 277 (2020) 124094, https://doi.org/10.1016/j.jclepro.2020.124094.

[36] W.Z. Hao, X. Tang, Y. Zhou, Recent Progress on mechanism of mechanical abuse, in: W.Z. Hao, X. Tang, Y. Zhou (Eds.), SAE Technical Paper Series, SAE International, 400 Commonwealth Drive, Warrendale, PA, United States, 2024.

[37] S. Hoelle, S. Scharner, S. Asanin, O. Hinrichsen, Analysis on thermal runaway behavior of prismatic Lithium-ion batteries with autoclave calorimetry, J. Electrochem. Soc. 168 (2021) 120515, https://doi.org/10.1149/1945-7111/ac3c27.

[38] V. Ruiz, A. Pfrang, A. Kriston, N. Omar, P. van den Bossche, L. Boon-Brett, A review of international abuse testing standards and regulations for lithium ion batteries in electric and hybrid electric vehicles, Renew. Sust. Energ. Rev. 81 (2018) 1427–1452, https://doi.org/10.1016/j.rser.2017.05.195.

[39] Phil Dilanni, BMW Group and Solid Power are testing all-solid-state battery cells in a BMW i7. https://www.press.bmwgroup.com/usa/article/detail/T0450262EN_US/bmw-group-and-solid-power-are-testing-all-solid-state-battery-cells-in-a-bmw-i7?language=en_US&utm_source=chatgpt.com, 2025. (Accessed 1 June 2026).

[40] Y. Zheng, S. Zhang, J. Ma, F. Sun, M. Osenberg, A. Hilger, H. Markötter, F. Wilde, I. Manke, Z. Hu, G. Cui, Codependent failure mechanisms between cathode and anode in solid state lithium metal batteries: Mediated by uneven ion flux, Sci. Bull. 68 (2023) 813–825, https://doi.org/10.1016/j.scib.2023.03.021.

[41] J. Zhang, C. Zheng, L. Li, Y. Xia, H. Huang, Y. Gan, C. Liang, X. He, X. Tao, W. Zhang, Unraveling the intra and intercycle interfacial evolution of Li_6PS_5Cl-based all-solid-state lithium batteries, Adv. Energy Mater. 10 (2020) 1903311, https://doi.org/10.1002/aenm.201903311.

[42] B. Lelotte, C.A.F. Vaz, L. Xu, C.N. Borca, T. Huthwelker, V. Pelé, C. Jordy, L. Gubler, M. El Kazzi, Spatio-chemical deconvolution of the $LiNi_{0.6}Co_{0.2}Mn_{0.2}O_2$/$Li_6PS_5Cl$ interphase layer in all-solid-state batteries using combined X-ray spectroscopic methods, ACS Appl. Mater. Interfaces 17 (2025) 14645–14659, https://doi.org/10.1021/acsami.4c19857.

[43] S.-J. Yang, J.-K. Hu, F.-N. Jiang, H. Yuan, H.S. Park, J.-Q. Huang, Safer solid-state lithium metal batteries: Mechanisms and strategies, InfoMat 6 (2024) e12512, https://doi.org/10.1002/inf2.12512.

[44] H. Komatsu, S. Banerjee, M.L. Holekevi Chandrappa, J. Qi, B. Radhakrishnan, S. Kuwata, K. Sakamoto, S.P. Ong, Interfacial stability of layered $LiNi_xMn_yCo_{1-x-y}O2$ cathodes with sulfide solid electrolytes in all-solid-state rechargeable lithium-ion batteries from first-principles calculations, J. Phys. Chem. C 126 (2022) 17482–17489, https://doi.org/10.1021/acs.jpcc.2c05336.

[45] BCE Special Ceramics, VERGLEICHSTABELLE TECHNISCHER KERAMIK. https://www.bce-special-ceramics.de/vergleich/bce-materialtabelle.htm, 2025. (Accessed 1 June 2026).

[46] Sto AG, Sto-Dämmplatte XPS 300 SO: Technisches Merkblatt. Exdrudierte Polystyrol Hartschaumplatte. https://www.stoag.ch/webdocs/productdocuments/TechnicalDataSheet_Sto-Daemmplatte_XPS_300_SO_0202_DE_01_00.PDF, 2025 (accessed 1 June 2026).

[47] Frank Kreith, Raj Manglik, Mark Bohn, Principles of Heat Transfer, seventh ed., Cl-Engineering, 2010.

[48] Y.-T. Chen, M.A.T. Marple, D.H.S. Tan, S.-Y. Ham, B. Sayahpour, W.-K. Li, H. Yang, J.B. Lee, H.J. Hah, E.A. Wu, J.-M. Doux, J. Jang, P. Ridley, A. Cronk, G. Deysher, Z. Chen, Y.S. Meng, Investigating dry room compatibility of sulfide solid-state electrolytes for scalable manufacturing, J. Mater. Chem. A 10 (2022) 7155–7164, https://doi.org/10.1039/D1TA09846B.

[49] Y. Liu, Y. Tian, Z. Fu, H. Du, B. Li, F. Kang, K. Amine, G. Chen, Thermite reaction-induced thermal runaway of lithium-ion batteries, Adv. Mater. 37 (2025) e10486, https://doi.org/10.1002/adma.202510486.

[50] H.-J. Noh, S. Youn, C.S. Yoon, Y.-K. Sun, Comparison of the structural and electrochemical properties of layered $Li[Ni_xCo_yMn_z]O2$ (x = 1/3, 0.5, 0.6, 0.7, 0.8 and 0.85) cathode material for lithium-ion batteries, J. Power Sources 233 (2013) 121–130, https://doi.org/10.1016/j.jpowsour.2013.01.063.

[51] L. Gan, R. Chen, X. Yang, X. Xu, M. Zan, Q. Li, Y. Wang, D. Su, X. Yu, H. Li, L. Chen, Comparative study on high-voltage safety performance of $LiNi_xMn_yCo_zO2$ cathode with different nickel contents, Appl. Phys. Lett. 121 (2022) 203901, https://doi.org/10.1063/5.0123625.

[52] Z. Tang, D. Feng, Y. Xu, L. Chen, X. Zhang, Q. Ma, Safety issues of layered nickel-based cathode materials for lithium-ion batteries: Origin, strategies and prospects, Batteries 9 (2023) 156, https://doi.org/10.3390/batteries9030156.

[53] R. LaFollette, M.D. Eskra, The possible role of thermite reactions in thermal runaway of Li-ion cells with layered cathodes, J. Electrochem. Soc. 171 (2024) 80509, https://doi.org/10.1149/1945-7111/ad6939.

[54] T.A. Yersak, H.J. Gonzalez Malabet, V. Yadav, N.P. Pieczonka, W. Collin, M. Cai, Flammability of sulfide solid-state electrolytes β-Li_3PS_4 and Li_6PS_5Cl: Volatilization and autoignition of sulfur vapor – New insight into all-solid-state battery thermal runaway, J. Energy Chem. 102 (2025) 651–660, https://doi.org/10.1016/j.jechem.2024.11.031.

[55] S.-M. Bak, E. Hu, Y. Zhou, X. Yu, S.D. Senanayake, S.-J. Cho, K.-B. Kim, K.Y. Chung, X.-Q. Yang, K.-W. Nam, Structural changes and thermal stability of charged $LiNi_xMn_yCo_zO_2$ cathode materials studied by combined in situ time-resolved XRD and mass spectroscopy, ACS Appl. Mater. Interfaces 6 (2014) 22594–22601, https://doi.org/10.1021/am506712c.

[56] H. Tsukasaki, W. Fukuda, H. Morimoto, T. Arai, S. Mori, A. Hayashi, M. Tatsumisago, Thermal behavior and microstructures of cathodes for liquid electrolyte-based lithium batteries, Sci. Rep. 8 (2018) 15613, https://doi.org/10.1038/s41598-018-34017-2.

[57] J. Hou, X. Feng, L. Wang, X. Liu, A. Ohma, L. Lu, D. Ren, W. Huang, Y. Li, M. Yi, Y. Wang, J. Ren, Z. Meng, Z. Chu, G.-L. Xu, K. Amine, X. He, H. Wang, Y. Nitta, M. Ouyang, Unlocking the self-supported thermal runaway of high-energy lithium-ion batteries, Energy Storage Mater. 39 (2021) 395–402, https://doi.org/10.1016/j.ensm.2021.04.035.